Nanoscale

PAPER

View Article Online
View Journal | View Issue

Cite this: *Nanoscale*, 2025, **17**, 25120

May the target be with you: polysaccharide-coated upconverting nanoparticles for macrophage targeting

Karolina Zajdel, *†[a] Volodymyr Lobaz, †[b] Martin Ondra, ‡[c,d] Rafal Konefał, [b,e] Oliver Moravec,[b] Ognen Pop-Georgievski, [b] Jiří Pánek, [b] Damian Kalita, [a] Bożena Sikora-Dobrowolska, [f] Lukáš Lenart, [c] Marián Hajdúch, [c,d] Martin Hrubý [b] and Marek Pruszyński [a,g]

Received 5th May 2025,
Accepted 1st September 2025

DOI: 10.1039/d5nr01833a

rsc.li/nanoscale

Upconversion nanoparticles (UCNPs) based on β-$NaYF_4$ doped with Yb^{3+} and Er^{3+} are promising candidates for multimodal bioimaging and theranostic applications, owing to their unique optical properties and favourable safety profile. However, their limited stability under physiological conditions and lack of effective cellular targeting continue to restrict their clinical translation. Here, we report a surface functionalisation strategy using hydroxybisphosphonate-modified polysaccharides—specifically mannan and inulin—to improve both colloidal stability and biological performance of UCNPs. Mannan with grafted hydroxybisphosphonate anchor groups formed a robust coating that prevented aggregation in phosphate-buffered and serum-containing media, while preserving upconversion luminescence. Crucially, the mannan-functionalised surface enabled selective interaction with mannose receptor (MR)-expressing macrophages (J774A.1), facilitating efficient cellular uptake as demonstrated by confocal microscopy and receptor inhibition assays. *In vitro* studies confirmed the high biocompatibility of mannan-coated UCNPs across a broad concentration range (0.5–10 μg mL^{-1}), with no significant cytotoxicity or oxidative stress observed. This streamlined and effective surface modification approach yields a stable, receptor-targeted nanoplatform with strong potential for future *in vivo* diagnostic and therapeutic applications involving immune cells.

Introduction

Nanoparticles have emerged as powerful tools in the field of diagnostics due to their unique physicochemical properties, including high surface area-to-volume ratio, tuneable surface chemistry, and the ability to interact with biological systems at the molecular level. These features enable enhanced sensitivity, specificity, and speed in detecting a wide range of biomarkers associated with diseases. Recent advancements in nanotechnology have facilitated the development of nanoparticle-based diagnostic platforms that integrate imaging, biosensing, and targeted detection, offering promising alternatives to conventional diagnostic methods, especially for cancers.[1,2]

Accurate imaging of contrast agents and therapeutics within diseased cells is critical for effective diagnosis and treatment. Radionuclide-based imaging methods, such as Single-Photon Emission Computed Tomography (SPECT) and Positron Emission Tomography (PET) combined with Computed Tomography (CT), offer high sensitivity and quantitative capabilities, while optical imaging provides a noninvasive, radiation-free alternative. However, conventional optical methods face limitations such as shallow tissue penetration and background autofluorescence. These challenges have spurred interest in near-infrared (NIR) optical imaging, particularly using lanthanide-doped upconversion nanoparticles (UCNPs), such as $NaYF_4$:Yb^{3+}/Er^{3+}.[3–6] These particles absorb NIR light and emit visible light, allowing deeper tissue imaging with minimal scattering and autofluorescence. In addition to these optical benefits, UCNPs exhibit several favourable properties for biomedical applications, including

[a]*NOMATEN Centre of Excellence, National Centre for Nuclear Research, A. Sołtana 7, 05-400 Świerk/Otwock, Poland. E-mail: kk.zajdel@gmail.com*
[b]*Institute of Macromolecular Chemistry of the Czech Academy of Sciences, Heyrovského n. 1888/2, 162 06 Prague 6, Czech Republic*
[c]*Laboratory of Experimental Medicine, Institute of Molecular and Translational Medicine, Faculty of Medicine and Dentistry, Palacky University and University Hospital, Olomouc, Czech Republic*
[d]*Institute of Molecular and Translational Medicine, Czech Advanced Technology and Research Institute, Palacky University Olomouc, Czech Republic*
[e]*NanoBioMedical Centre, Adam Mickiewicz University, Wszechnicy Piastowskiej 3, 61-614 Poznań, Poland*
[f]*Institute of Physics Polish Academy of Sciences, Aleja Lotników 32/46, 02-668 Warsaw, Poland*
[g]*Institute of Nuclear Chemistry and Technology, Dorodna 16, 03-195 Warsaw, Poland*
†These authors contributed equally to this work.

high resistance to photobleaching and photoblinking, superior signal-to-noise ratio, large anti-Stokes shifts, narrow emission bands, long luminescence lifetimes, and outstanding photo- and chemical stability. Furthermore, they generally demonstrate low cytotoxicity and minimal photodamage to biological tissues, supporting their use in advanced diagnostic and therapeutic strategies.[7,8]

UCNPs also show great promise in theranostic applications, combining multimodal imaging, targeted drug delivery, and phototherapies within a single platform.[6,9–14] This multifunctionality holds significant potential for enhancing detection sensitivity and enabling personalized treatment strategies tailored to individual patients. Nonetheless, clinical translation remains limited due to several physicochemical and biological challenges. Despite their chemical stability, recent studies have shown that UCNPs may undergo partial dissolution in biological media, potentially compromising their performance and safety.[15–17] There is also a question that upconversion yield increases with square of light intensity, which requires the use of high light fluxes, so such systems are more appropriate for diagnostic imaging than for therapeutic applications. Therefore, the development of next-generation nanomaterials that combine strong optical performance, high biocompatibility, and efficient clearance from the body is crucial. A deeper understanding of their interactions within biological systems will be essential for unlocking their full clinical potential.

Surface biofunctionalisation plays a pivotal role in determining the interactions of UCNPs with biological systems, and is thus a critical aspect of their application in the life sciences. The surface coating material influences the nanoparticles' physicochemical properties, affecting both their performance and versatility. Effective biofunctionalisation ensures not only biocompatibility—by minimizing cytotoxicity and optimizing dose–response behaviour—but also promotes targeted cellular interactions and internalization. Furthermore, the coating must confer colloidal stability, enabling the nanoparticles to perform consistently across various environments, from *in vitro* studies to future *in vivo* applications. Despite its importance, achieving a functional and stable biofunctionalised nanoparticle system remains a significant challenge, particularly when addressing long-term storage stability.[18,19]

Polysaccharides like mannan (MN) show promise as platforms for diagnostic probes, not only in cancer detection but also for identifying cancer-related complications such as sentinel lymph node (SLN) involvement.[20–22] SLNs, the first nodes to receive metastatic cells from primary tumours, are crucial for staging cancers like breast, prostate, and melanoma. Although sentinel lymph node biopsy is less invasive than full dissection, it still carries surgical risks. Emerging imaging techniques, including Magnetic Resonance Imaging (MRI), SPECT/MRI, and PET/NIRF, show potential but remain supplementary tools. This highlights the need for new, effective SLN-targeted diagnostic approaches.

The MN from *Saccharomyces cerevisiae* is a biocompatible, modifiable polysaccharide for multimodal probe development. MN naturally binds to mannose receptors, particularly those on dendritic cells and macrophages that populate inflamed or cancer-infiltrated lymph nodes.[20–22] These properties make MN a strong candidate for targeted imaging and potential therapeutic strategies.

Mannose receptors (MRs) are a class of pattern recognition receptors (PRRs) primarily expressed on the surface of macrophages, dendritic cells (DCs), and selected endothelial cells, where they play a central role in innate immunity.[23,24] These transmembrane C-type lectin receptors recognize carbohydrate structures rich in mannose, fucose, and *N*-acetylglucosamine, commonly found on the surfaces of pathogens. In macrophages and DCs, MRs mediate endocytosis and phagocytosis of glycosylated antigens, facilitating antigen processing and presentation to T cells, thereby bridging innate and adaptive immune responses. Particularly, the MR subtype CD206 is highly expressed on alternatively activated (M2) macrophages and immature DCs, where it contributes to tissue remodelling, immune regulation, and pathogen clearance.[25] Moreover, dendritic cells overexpressing DC-SIGN (dendritic cell-specific intercellular adhesion molecule-3-grabbing non-integrin), another mannose-binding receptor, are pivotal in capturing mannose-rich antigens and promoting T-cell activation.[24] These characteristics make mannose receptors valuable targets for delivering diagnostic or therapeutic agents to immune cells, especially within inflamed tissues or tumour-draining lymph nodes.

Recently, we developed polysaccharide-coated calcium tungstate and tungsten(VI)oxide nanoparticles where the polysaccharides, including MN, were directly bound on the surface by direct chelation to calcium and tungsten.[26] However, the coating was not completely stable.

To prevent dissolution, preserve luminescence, and minimize the potential toxicity of lanthanide-doped $NaYF_4$ UCNPs, it is essential to apply a protective surface coating. Among various options, phosphonate groups are considered highly effective anchoring agents due to their strong binding affinity to lanthanide (Ln) ions, which helps passivate the particle surface and prevent degradation under biological conditions. While poly(ethylene oxide)-phosphonate-modified lanthanide-doped $NaYF_4$ UCNPs bearing a single reactive group can form stable colloids in water, they tend to aggregate in phosphate-buffered saline (PBS). In contrast, we have shown that poly (ethylene oxide)-hydroxybisphosphonate ligands establish robust, multidentate interactions with Ln ions, ensuring long-term colloidal stability of UCNPs in both water and PBS. This stable nanoparticle surface modification using poly(ethylene oxide) conjugated *via* hydroxybisphosphonate (HBP) linkers, offers a promising route to enhance biocompatibility and stability for biomedical applications.[4]

In this paper, we report—for the first time to the best of our knowledge—the combination of mannan's potent macrophage-targeting properties with the excellent multimodal imaging capabilities of UCNPs. This is achieved through the use of a hydroxybisphosphonate anchoring group, enabling a simple, mix-and-use approach for nanoparticle coating with the polysaccharide mannan. Mannan offers a significant

advantage over single D-mannose targeting units[3,27,28] due to its multivalent nature, possessing numerous D-mannose residues that allow for synergistic, high-affinity binding to mannose receptors. These receptors, as members of the lectin family, feature multiple saccharide-binding domains. The flexible backbone of the MN chain ensures steric accessibility to receptor binding sites, while its macromolecular nature provides effective steric and colloidal stabilization of nanoparticles—capabilities not achievable with monovalent D-mannose derivatives. To facilitate stable and direct attachment to UCNPs surface, MN was functionalised with HBP groups. This approach also allows modular co-functionalization with other HBP-linked molecules in a toolbox manner.[4] The UCNPs were doped with lanthanides (2 mol% Er and 20 mol% Yb) to confer appropriate upconversion fluorescence properties in the NIR range for imaging purposes. Additionally, the lanthanide doping enhances X-ray opacity for potential future use in CT imaging and enables neutron activation, supporting theranostic applications (internal radiotherapy + SPECT) such as the elimination of sentinel lymph node-associated metastases (see Fig. S1, SI for an example of calculated direct thermal neutron activation).

Results and discussion

Synthesis of UCNP-C and UCNP-S

Core β-$NaYF_4$:20%Yb^{3+},2%Er^{3+} (UCNP-C) and core–shell β-$NaYF_4$:20%Yb^{3+},2%Er^{3+}@$NaYF_4$ (UCNP-S) UCNPs were synthesised *via* a thermal decomposition approach using organic lanthanide precursors, as previously demonstrated.[29,30] The reaction conditions were carefully optimised to obtain monodisperse nanocrystals with uniform morphology and mean diameters of approximately 25.3 ± 2.7 nm and 39.1 ± 3.5 nm for UCNP-C and UCNP-S, respectively (Fig. 1A and B). The resulting nanostructures comprised Yb^{3+} and Er^{3+} dopant ions embedded within a sodium yttrium fluoride ($NaYF_4$) matrix, a well-established host for upconversion luminescence. Among the UCNPs structures reported in the literature, the hexagonal (β) phase of $NaYF_4$ is considered the most efficient due to its low phonon energy (~350 cm^{-1}),[31] which reduces non-radiative relaxation.

The applied synthesis protocol enabled the reproducible preparation of high-quality β-$NaYF_4$ UCNPs with controlled size, shape, and phase purity, making them highly promising for biomedical applications such as multimodal imaging,[32] nanoprobing for biomolecular detection, drug delivery,[33] cancer therapy,[34] and theranostics,[35] thereby attracting significant research interest.[30,36–40] The morphology and structure of UCNP-C and UCNP-S were characterized by transmission electron microscopy (TEM) and scanning electron microscopy (SEM). Selected area electron diffraction (SAED) confirmed the hexagonal (P6) crystal structure of $NaYF_4$ Energy-dispersive X-ray spectroscopy (EDS) confirmed the presence of all expected elements in the sample, with Na, Y, and F being the predominant constituents, consistent with the composition of the $NaYF_4$ host matrix (Fig. S2, SI). High-resolution transmission electron microscopy (HR-TEM, Fig. 1E and F) showed distinct lattice fringes with an interplanar spacing of 5.16 Å, indicative of the crystalline nature of the obtained nanoparticles. The observed periodicity suggests a highly ordered atomic arrangement, consistent with previously reported β-phase $NaYF_4$ upconversion nanomaterials.[29,41]

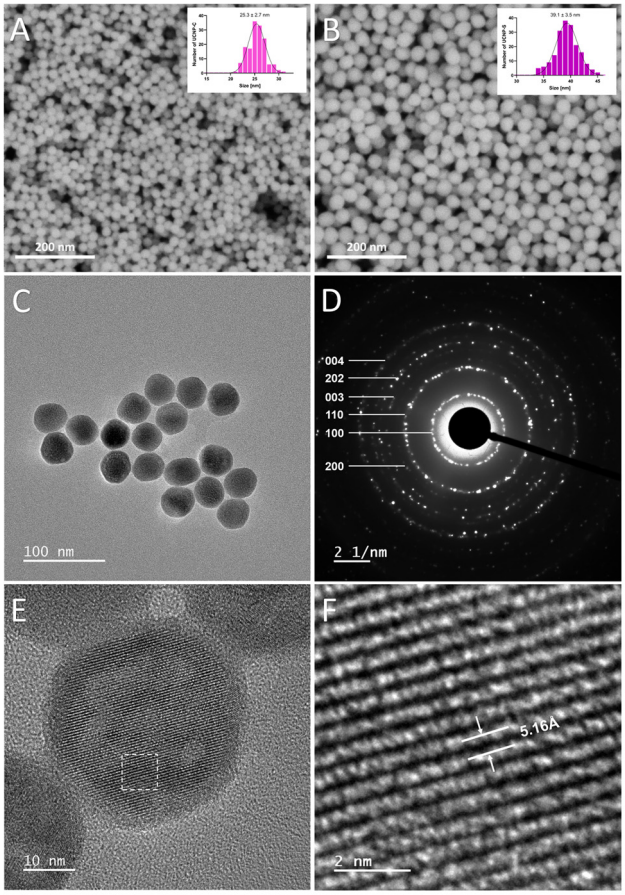

Fig. 1 SEM images of UCNP-C (A) and UCNP-S (B). BF TEM image (C), SAED pattern (D), HR TEM (E) and magnified HR TEM (F) images of$NaYF_4$:Yb,Er@$NaYF_4$ UCNP-S.

Polysaccharides coatings

UCNPs exhibit significant potential for *in vivo* applications; however, their colloidal and chemical stability in physiological media is compromised, and UCNPs rapidly aggregate in phosphate-containing environments, resulting in the loss of their optical properties as the particles degrade.

To prevent immediate aggregation, an effective protective coating is required. A promising approach involves the use of polymers functionalized with hydroxybisphosphonate moieties. These moieties exhibit a strong affinity for the nanoparticle surface, while the polymer itself provides steric or electrostatic repulsion, thereby enhancing colloidal stability.[4,42]

For the development of a functional protective coating on UCNPs, two non-ionic branched polysaccharides were selected:

inulin, an inert fructose-based polymer, and mannan, a mannose-based polymer with the potential to target MRs. Both polysaccharides were chemically modified by grafting sodium neridronate through oxidation of a diol group within the saccharide ring to form an aldehyde. This was followed by Schiff base formation with the amine group of neridronate, and its subsequent reduction to a secondary amine using sodium cyanoborohydride (Fig. 2A).

Physicochemical characterization of polysaccharide-coated UCNPs

The theoretical proportion of saccharide monomer units (SMUs) subjected to oxidation for neridronate grafting was 10% and 30% on a molar basis, and the grafting yield was monitored using ^{1}H NMR spectroscopy. The spectra of pristine inulin and mannan are presented in (Fig. S3, SI), where each SMU contains six protons, resulting in multiple overlapping peaks within the 3.5–5.5 ppm range. In contrast, the neridronate molecule exhibits characteristic signals from five methylene groups within the 3.0–1.0 ppm region (Fig. 2B). Specifically, the peak at 3.03 ppm, attributed to the methylene group in the α-position relative to the amine group of neridronate, was compared with the peak at 4.21 ppm from H-3 of the fructose ring in inulin, as well as with the peaks at 5.26 ppm and 5.06 ppm from H-1 of the mannose ring in mannan.

The degree of Ner grafting, expressed as the molar percentage of SMU carrying a single Ner moiety, is summarized in Table 1. Although oxidation of a single saccharide ring theoretically generates two functional groups capable of binding Ner, the actual grafting efficiency was significantly lower. Inulin demonstrated lower susceptibility to oxidation by sodium periodate, yielding 3.6 mol% of SMU carrying Ner (I-10 sample), compared to 6.7 mol% in mannan under identical reaction conditions (M-10 sample). Furthermore, the fraction of SMU susceptible to oxidation and subsequent modification was substantially below 100%. Notably, an attempt to oxidize and modify 30 mol% of SMU in M-30 mannan sample resulted in a grafting efficiency comparable to that observed at 10%, suggesting a saturation effect in the modification process. The trends in Ner grafting to inulin and mannan were further confirmed by determining the phosphorus content in the samples (Table 1).

Next, polysaccharide samples grafted with Ner were labelled with AF 488 fluorescent dye using a spacer terminated with an amine *via* the same reductive amination pathway described previously for Ner grafting. Oxidation was performed on 8 mol% of SMU, yielding 0.08–0.29% of SMUs carrying the AF 488 dye (Table 1). The low grafting efficiency observed in this second modification cycle further confirms the limited availability of SMUs susceptible to oxidation under the given reaction conditions.

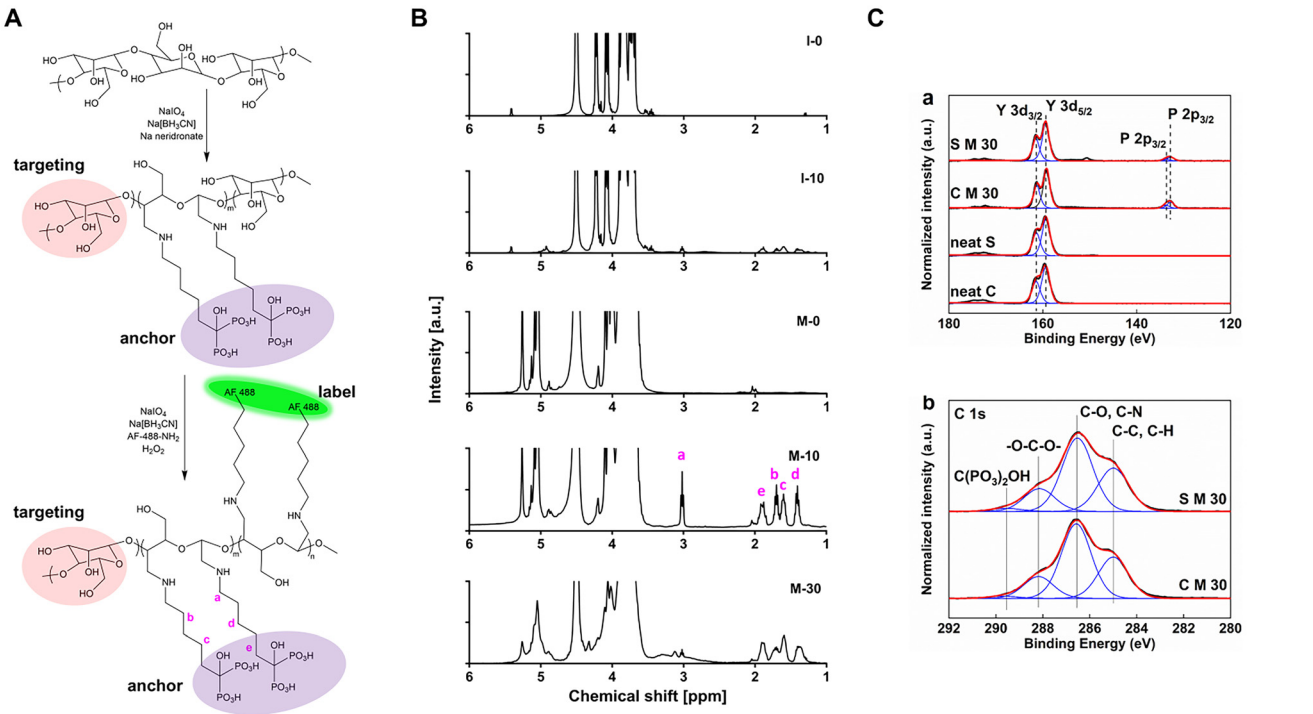

Fig. 2 Scheme of modification of mannan with anchor hydroxybisphosphonate groups and AF 488 fluorescent label (A); ^{1}H NMR spectra of mannan and inulin with grafted sodium neridronate groups (B). For the assignment of protons in pristine inulin and mannan see Fig. S3, SI. (C) (a) Comparison of high resolution XPS spectra of neat core and core/shell $NaYF_4$ nanoparticles before and after the anchoring of M30 through Ner anchoring groups; (b) representative C 1s high resolution XPS spectra of core and shell nanoparticles bearing M30. (Black: measured data; red: fitted data; blue: individual contributions of functional groups.)

Table 1 Composition and molecular weight distributions of mannan and inulin with grafted Ner and AF 488

	SEC					Elemental analysis		
Sample[a]	M_n, Da	M_w, Da	$Đ$	DP[b] (SEC)	Ner,[c] % (^{1}H NMR)	P, %	Ner,[c] %	AF 488,[d] % (UV-Vis)
I-0	2630	5250	2.0	15	n/a			
I-10	2220	4361	2.0	14	3.6	1.0	2.6	0.08
M-0	20 120	33 020	1.6	124	n/a			
M-10	6770	13 980	2.1	42	6.7	3.3	8.9	0.29
M-30	Not measurable[e]			n/a	4.4	3.4	9.2	0.15

[a] Samples are labelled with M (mannan) and I (inulin) followed with a number, corresponding to a calculated molar % of SMU, oxidized for grafting Ner molecule (see Fig. 2A). [b] M_n, obtained from SEC, divided by a molecular weight of a saccharide monomer unit (162.14). [c] Calculated as a molar % of saccharide units, carrying one Ner molecule (see the discussion in the NMR section). [d] Calculated as a molar % of saccharide units, carrying one AF 488 molecule, similar to Ner. [e] Sample fluorescence.

The precise determination of molecular weight for branched polysaccharides is challenging; however, size-exclusion chromatography (SEC) enables monitoring of molecular weight (M_w) changes while keeping all other parameters constant. The M_w of pristine polysaccharides was higher than that of those modified with Ner and AF 488. Inulin exhibited only a minor decrease in M_w, consistent with its lower susceptibility to oxidation and modification. In contrast, mannan with 10% oxidized SMU showed a threefold reduction in M_w. The M-30 sample, in which 30% of SMU was oxidized, could not be measured due to fluorescence interference.

The chemical composition of the neat UCNP-C and UCNP-S was proven *via* XPS analysis (Fig. 2C). The high-resolution XPS spectra of both types of nanoparticles showed the presence of the dominant Y 3d double peak at 159.3 eV (with a characteristic Y $3d_{5/2}$ → Y $3d_{3/2}$ spin split doublet with a separation of 2.1 eV).[43] The ratio between the contributions of Na : Y : F (determined ratios of 1.4 : 1.0 : 4.3 and 1.3 : 1.0 : 5.2 for the core and shell particles, respectively) corresponds well to the expected theoretical stoichiometry of 1.0 : 1.0 : 4.0 of $NaYF_4$ (Table S1, SI). In the high-resolution spectra taken in the C 1s region of neat particles we observed contributions originating from oleic acid (spectra not shown). The immobilization of mannan and inulin polysaccharides bearing neridronate anchoring groups led to a distinct change in the chemical composition of both types of UNCPs. Namely in the region of 180–120 eV, covering the Y 3d, Si 2s and P 2p regions we observed a drop in the intensity of Y 3d and the appearance of P 2p signals of the neridronate group at 132.8 eV (with a characteristic P $2p_{3/2}$ → P $2p_{1/2}$ spin split doublet with a separation of 1.0 eV) (Table S1, SI). Concomitantly we have observed the appearance of nitrogen signals of N–C moieties at 400.0 eV (these are highly overlapped with the Y 3s signals of the solid part of the particles and the quantification might be troublesome). However, in the C 1s spectra of the modified UNCPs we observe the dominance of the C–O (and C–N) contributions at 286.5 eV stemming from the hydroxy groups of the saccharide moieties, –O–C–O– structures at 288.0 eV of various β(1-4) and β(2-1) linkages present in the polysaccharides, and the anchoring $(PO_3H)_2C$–OH moiety at 289.5 eV. The presence of the $(PO_3H)_2C$–OH moiety is also well reflected in the quantitative assessment of the data, *i.e.* being in quite good agreement with the N–C moieties observed in the N 1s spectra as well as in the phosphonate signals of P 2p (Table S1, SI).

The fluorescence of AF 488 was used to determine the diffusion coefficient of the fluorophore by Fluorescence Correlation Spectroscopy (FCS) (Table 2). For all samples, two-component correlation curves were observed. After deconvolution of the correlation curves two diffusion coefficients were obtained: a fast diffusion, ranging from 78 to 260 $\mu m^2\ s^{-1}$, which corresponds to the admixture of a free dye or free labelled polysaccharide, and a slow diffusion component, ranging from 5.5 to 47.8 $\mu m^2\ s^{-1}$. The latter is attributed to nanoparticles carrying labelled polysaccharide on the surface. The number-average hydrodynamic diameters of the corresponding nanoparticles are consistent with those measured by SEM (UCNPs without polymer coating, Fig. 1A and B) and DLS (UCNPs with polysaccharides in cell culture medium, Fig. 3B).

The upconversion emission of 1 mg mL^{-1} UCNP-C and UCNP-S, along with the emission from an AF 488 label in the polysaccharide shell, is shown in Fig. 3A. The upconverting properties were fully preserved after the adsorption of polysaccharides, mediated by the hydroxybisphosphonate moiety.

The colloidal stability of UCNP-C and UCNP-S coated with I-10, M-10, and M-30 was evaluated at 37 °C in DMEM culture medium containing 10% fetal bovine serum (FBS). Stability was assessed by measuring the hydrodynamic diameter every 30 min over 12 h. The exact dimensions of the UCNPs were determined from SEM micrographs (Fig. 1). To monitor nano-

Table 2 Diffusion coefficients and number-average hydrodynamic diameters of core and core–shell UCNPs coated with inulin and mannan, labelled with AF 488, measured by FCS

UCNPs	Polysaccharide coating	D_1 ($\mu m^2\ s^{-1}$)	d_n (nm) FCS	d_n (nm) SEM	D_2 ($\mu m^2\ s^{-1}$)
UCNP-C	I-10	11.3	38	25.1	260
	M-10	5.5	78		78
	M-30	47.8	9		210
UCNP-S	I-10	11.3	38	39.1	254
	M-10	12.0	35		163
	M-30	18.3	24		172

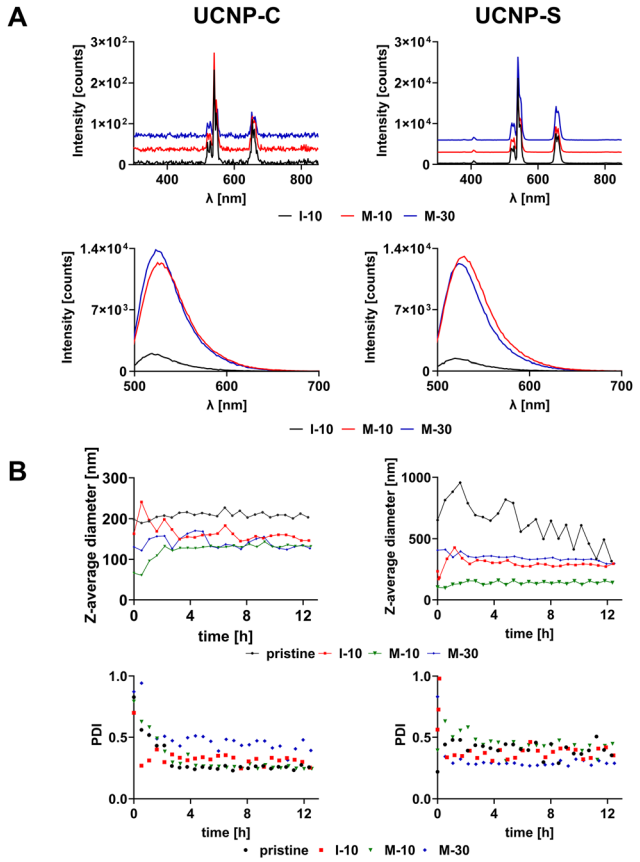

Fig. 3 (A) Dual mode emission spectra of UCNP-C and UCNP-S coated with inulin and mannan, labelled with AF 488 in DMEM. The upper plots show the characteristic upconversion emission of UCNPs centered around 520–540 nm and 660 nm (excited using a CW laser at 980 nm), while the lower plots present the fluorescence emission of AF 488 (centered around 520 nm). (B) The evolution of hydrodynamic diameter of UCNP-C and UCNP-S in DMEM culture medium with 10% of FBS with time at 37 °C.

particle behavior in DMEM, the *Z*-average hydrodynamic diameter, polydispersity index (PDI), derived count rate, and intensity-weighted size distributions of UCNPs were analysed. The *Z*-average diameter offers a single representative value for all nanoparticle populations in the system, making it highly sensitive to aggregation. Pristine UCNPs—both core and core–shell—exhibited larger hydrodynamic diameters compared to surface-modified UCNPs, suggesting a degree of aggregation in DMEM (Fig. 3B). This aggregation appears to be partially mitigated by serum proteins from FBS, which likely contribute to UCNP stabilization throughout the experiment. In contrast, pristine UCNPs in pure PBS precipitated within minutes. For UCNP-C the decrease in PDI (Fig. 3B) and an increase in the derived count rate (Fig. S5, SI) were recorded within the first three hours, pointing to equilibration of NPs with medium. But across all coatings and time points, the intensity-weighted size distributions of UCNP-C showed a dominant population at 100–200 nm, with only minor fractions of larger aggregates (Fig. S6, SI). In comparison, the derived count rate for UCNP-S fluctuated more significantly. Both uncoated UCNP-S and those coated with inulin (I10) showed signs of aggregation in the size distributions (Fig. S6, SI), although their *Z*-average diameters and PDI stabilized within the first two hours after mixing, and the main population near 200 nm persisted throughout the measurement period. UCNP-S coated with mannans remained colloidally stable. Overall, all three polysaccharide coatings contributed to maintaining colloidal stability of the UCNPs during the experiment. However, for UCNP-S, mannan coatings demonstrated significantly greater stabilizing effectiveness after mixing UCNPs with DMEM; however, after this period, both the *Z*-average diameter and PDI remained constant, suggesting that these coated UCNPs are suitable for *in vitro* experiments. Additionally, photoluminescence measurements performed for bare core–shell β-$NaYF_4$:20%Yb^{3+},2%Er^{3+}@$NaYF_4$ UCNPs dispersed in cyclohexane (Fig. S4, SI) revealed strong green and red upconversion luminescence under 980 nm laser excitation, confirming the high optical quality of the uncoated nanoparticles.

In vitro studies

As an initial step in the biological evaluation of the novel UCNPs, cytotoxicity was assessed using a cell viability (MTS) assay. J774A.1 murine macrophage tumour cells were employed as a model to investigate nanoparticle-induced cytotoxicity and cellular uptake. This cell line was chosen due to its heterogeneous surface expression of functional MRs,[44] which reflects the diversity typically observed among macrophage populations.[45]

No significant cytotoxicity was observed after 24 or 48 h of incubation with all variants of UCNPs at concentrations ranging from 0.5 to 10 μg mL^{-1} (Fig. 4A and B), confirming their biocompatibility. To evaluate the impact of UCNPs on oxidative stress, intracellular levels of reduced glutathione (GSH) were measured using the GSH Glo™ Glutathione Assay. A slight, dose-dependent decrease in GSH levels was detected (Fig. 4C), indicating mild oxidative stress; however, these changes were not statistically significant. To further investigate the reduction in GSH levels and to exclude a potential increase in reactive oxygen species (ROS), intracellular hydrogen peroxide (H_2O_2) levels were measured in J774A.1 cells following 24 h of UCNPs treatment. In the presence of a positive control (menadione),[46] a marked increase in H_2O_2 production was observed, reaching up to a 24-fold change. In contrast, none of the UCNPs treatments induced a significant increase in H_2O_2 levels (Fig. 4D).

To validate the theoretical prediction that mannan coating enhances UCNPs uptake in macrophages *via* MR-mediated endocytosis, J774A.1 cells were incubated with UCNPs at concentrations of 1, 5, and 10 μg mL^{-1} for 24 h. Uptake was assessed by detecting green fluorescence from AF 488 conjugated to the surface of UCNP-C and UCNP-S functionalised with either inulin (C-I10, S-I10) or mannan (C-M10, C-M30, S-M10, S-M30).

Confocal fluorescence microscopy imaging of live cells after 24 h of incubation revealed superior uptake of both C-M30

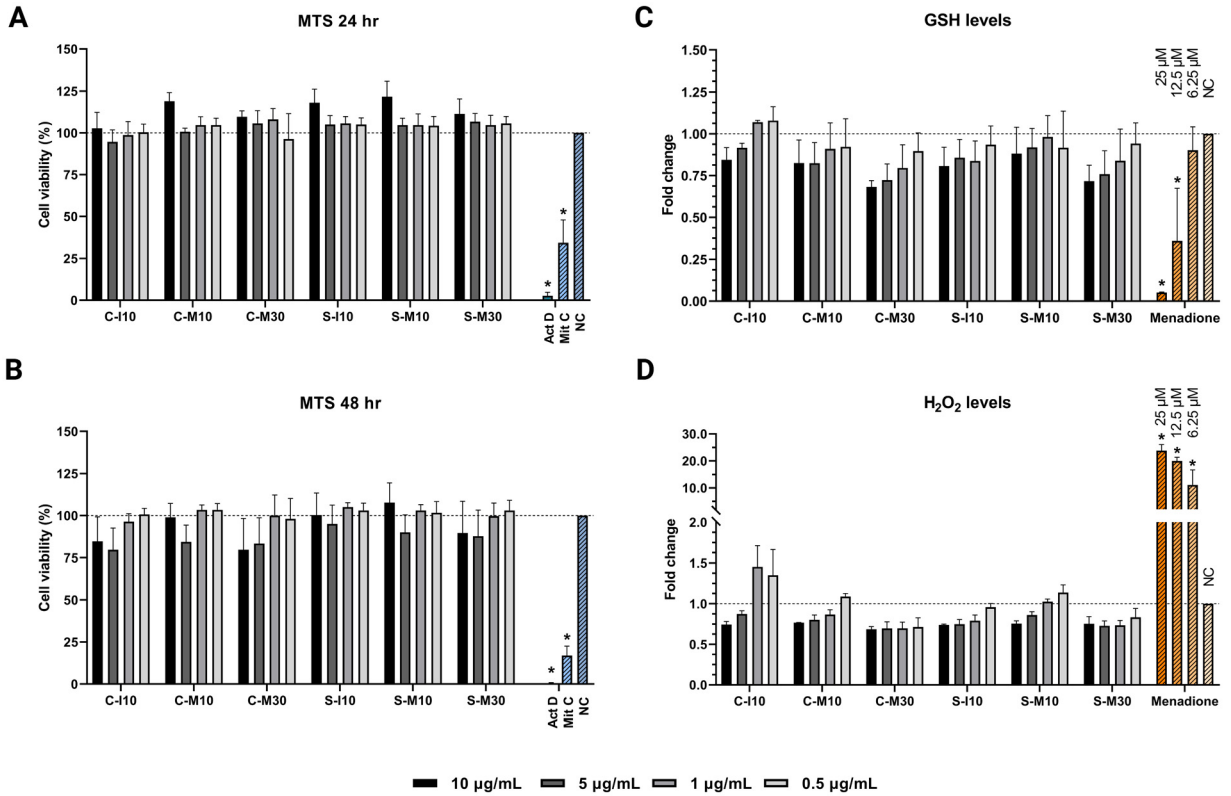

Fig. 4 Cell viability and oxidative stress levels in J774A.1 cells exposed to different types of UCNPs (C-I10, C-M10, C-M30, S-I10, S-M10, S-M30). The effect of UCNPs on cell viability after 24 (A) and 48 h (B), cellular levels of GSH (C), and H_2O_2 (D) after exposure of cells to different concentrations of UCNPs (0–10 μg mL^{-1}) (mean ± SD, n = 3). Negative controls (NC) – cells without treatment. MTS positive controls: 10 μM actinomycin D (Act D) and 10 μM mitomycin C (Mit C); ROS and GSH positive controls – 6.25; 12.5 and 25 μM menadione. P-Values were calculated using one-way ANOVA—Dunnett's test, * $p < 0.0001$.

and S-M30 compared to other UCNPs types tested (Fig. 5A). These findings were further corroborated after the cells were washed and fixed, effectively removing potentially non-internalized free UCNPs (Fig. 5B). Quantification of mean fluorescence intensity from three representative images for each treatment condition confirmed enhanced uptake of mannan-coated UCNPs (C-M30, S-M30) compared to the corresponding controls, C-I10 and S-I10, respectively (Fig. 5C). To evaluate the kinetics of UCNPs uptake, time-lapse live-cell imaging was conducted at 2-hour intervals (Fig. S7, SI). Signals for C-M30 and S-M30 were detectable in live cells as early as 2 h post-incubation.

To further verify both the internalization and luminescent properties of the UCNPs, confocal fluorescence imaging was performed using a microscope equipped with a near-infrared (980 nm) laser to excite upconversion emission (Fig. 6). The AF 488 signal (green channel) overlapped with the UCNP emission (red channel), providing strong evidence for successful mannan functionalization (Fig. 6B). The red signal from the UCNPs confirmed efficient cellular uptake and the preservation of their upconversion luminescence. Notably, S-M30 exhibited clear colocalisation with Rab7-positive endosomes after 4 h of incubation (Fig. 6A), indicating active endo–lysosomal trafficking.

These observations are consistent with previous studies indicating that the internalization of core–shell $NaYF_4$:Yb, Er@$NaYF_4$ UCNPs, functionalized with various copolymers and commercially available PAA and PEI polymers, occurs *via* clathrin-mediated endocytosis in J774A.1 macrophage cells.[47] In contrast, the uptake and toxicity of similar core UCNPs, such as $NaYF_4$:18%Yb,2%Er (33 ± 2 nm) with silica coatings, have been primarily assessed in RAW 264.7 macrophages.[48] In the context of active targeting of M2-type RAW 264.7 macrophages, mannose-decorated, macrophage membrane-coated, silica-layered $NaErF_4$@$NaLuF_4$ UCNPs, co-doped with perfluorocarbon (PFC)/chlorin e6 (Ce6) and loaded with paclitaxel (PTX), were successfully developed as a macrophage reprogramming. Furthermore, alternative polysaccharides, including guar gum, have been explored for their effects on the colloidal stability of $NaGdF_4$:Er^{3+}, Yb^{3+}-based UCNPs, as well as their influence on cellular uptake and cytotoxicity toward J774A.1 macrophages, demonstrating good dispersibility in biologically relevant media, chemical and optical stability, and high biocompatibility.[49]

To ensure that the observed red signal originated from UCNP upconversion rather than fluorescence bleed-through or cellular autofluorescence, lambda (λ) scans were conducted. The intracellular emission spectra (Fig. 6C), recorded in λ-scan mode upon 980 nm excitation, matched those obtained during

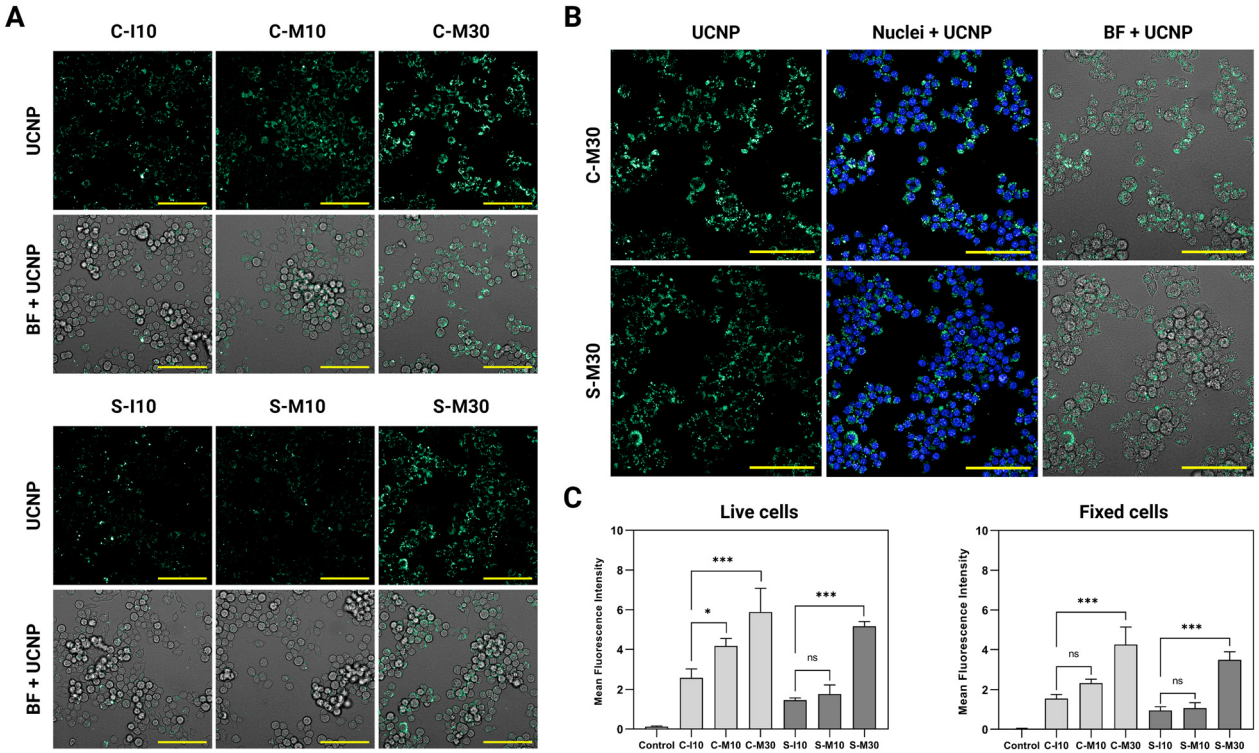

Fig. 5 Internalization of UCNPs. (A) Live-cell imaging of J774A.1 after 24 h incubation with 5 μg mL^{-1} of UCNPs. (B) Fixed cells with nuclei stained by Hoechst 33342 (blue channel). Green channel: AF 488 signal of UCNPs; BF: bright-field. (C) Quantification of UCNPs uptake calculated as the mean fluorescence intensity value per field. *P*-Values were calculated using ordinary one-way ANOVA—Tukey's test, * $p < 0.05$; *** $p < 0.001$; $n = 3$. Scale bar: 100 μm.

physicochemical characterization of the UCNPs,[29,30] displaying characteristic emission peaks at ~550 nm and ~660 nm, corresponding to green and red luminescence, respectively. To assess the intracellular biodistribution of UCNPs in J774A.1 cells, supplementary confocal microscopy was performed using *Z*-stack scanning followed by 3D reconstruction of the imaged section (Fig. S8, SI).

We observed that the fluorescence from internalized UCNPs is dominated by red emission at 655 nm (Fig. 6C), both in cells incubated with mannan-coated UCNPs and in colloidal dispersions of uncoated UCNPs in cyclohexane (Fig. S4). In contrast, UCNPs coated with mannan or inulin and dispersed in DMEM exhibit predominantly green emission at 540 nm (Fig. 3A). One possible explanation for the predominance of red emission observed in Fig. 6C is the use of femtosecond pulsed excitation, whereas the green-dominated spectra were obtained under continuous-wave (CW) excitation in cell medium. These different excitation regimes are known to affect the upconversion emission profile. For $NaYF_4$:Yb^{3+},Er^{3+} UCNPs, femtosecond pulsed excitation typically leads to a relative enhancement of red emission ($^4F_{9/2} \rightarrow {}^4I_{15/2}$ transition at ~655 nm) compared to green emission ($^2H_{11/2}$ and $^4S_{3/2} \rightarrow {}^4I_{15/2}$ transitions at ~520 and ~540 nm, respectively), as previously reported in the literature.[50,51]

Moreover, from a biological standpoint, the observed shift in dominant emission from green (~540 nm) in colloidal suspension (Fig. 3A) to red (~655 nm) after cellular internalization (Fig. 6C) can be explained by changes in the local chemical environment affecting how different Er^{3+} excited states respond to surface quenching. In protein-rich media such as DMEM supplemented with 10% FBS, there is a protein corona around the nanoparticles. This corona passivates surface defects and limits the interaction of high-energy vibrational groups (such as –OH, –NH_2, and –COOH) with the lanthanide ions. These groups are known to induce quenching of excited lanthanide states *via* multiphonon relaxation processes.[52] The protective corona could reduce non-radiative relaxation pathways. It may particularly shield the green-emitting states ($^2H_{11/2}$ and $^4S_{3/2}$), which are more sensitive to surface quenching than the red-emitting $^4F_{9/2}$ level, thereby enhancing green luminescence.[53] After internalization into cells, the nanoparticles encounter a more complex intracellular environment characterized by lower pH, enzymatic activity, and potential nanoparticle aggregation. These conditions facilitate the return of surface quenching mechanisms—especially multiphonon relaxation and cross-relaxation—that more strongly suppress green emission. Notably, although the red-emitting level is more resistant to these non-radiative decay processes, it is still significantly quenched, leading to the observed shift toward red-dominant emission inside the cell. Consequently, it can be inferred that both the adsorption of serum proteins and the nature of the surface coating, especially the not fully

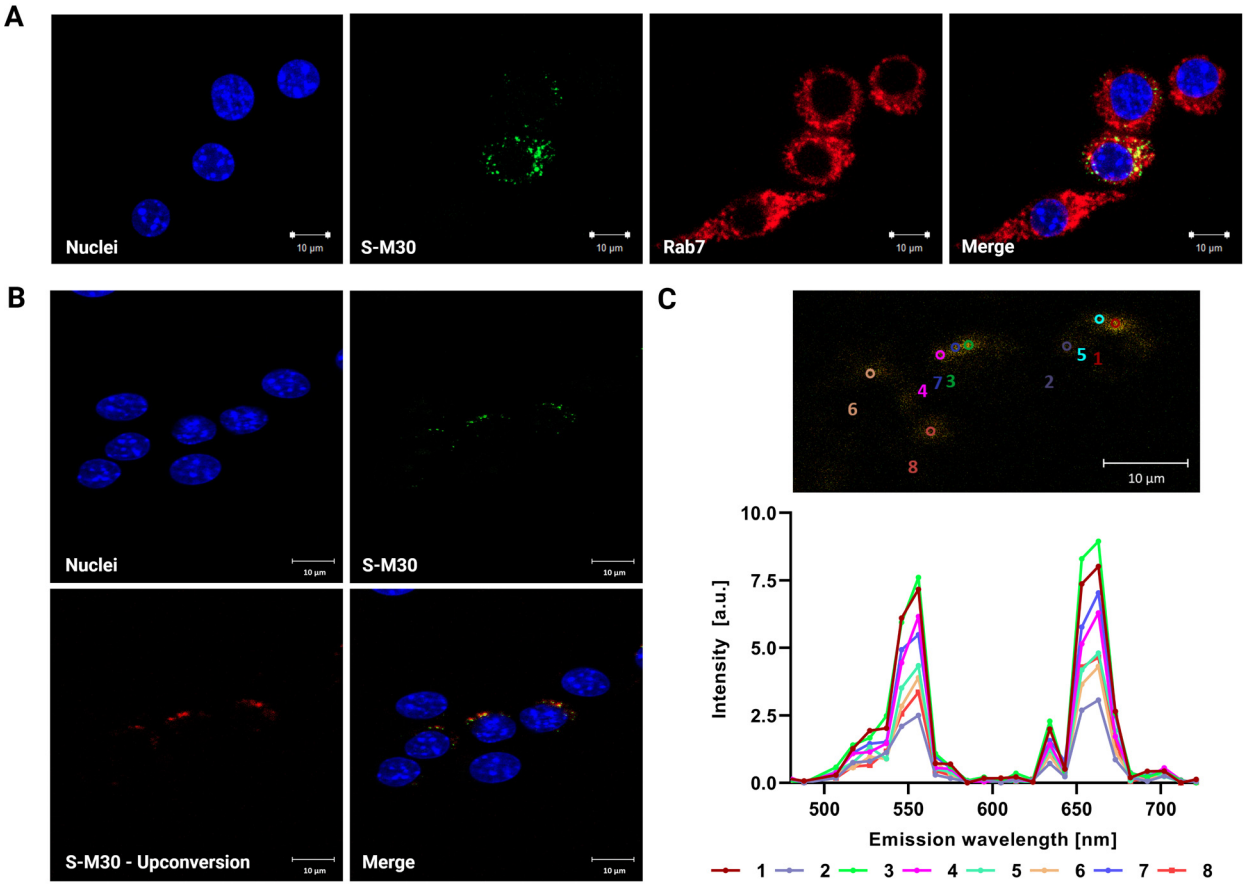

Fig. 6 Colocalization of UCNPs with late endosomes and confirmation of upconversion luminescence. (A) Confocal microscopy images showing colocalization of late endosomes (Rab7, red channel) with S-M30 (green channel represents AF 488 signal). (B) Confocal microscopy images of J774A.1 cells incubated with S-M30 for 4 h, confirming upconversion luminescence. Red channel: S-M30 luminescence (excited using a femtosecond laser at 980 nm); green channel: AF 488 signal of S-M30; blue channel: nuclei (Hoechst 33342). (C) Representative emission spectra of UCNPs recorded in λ-scan mode. n = 3. Scale bar: 10 μm.

characterized protein corona, and the dispersion environment significantly affect the relative intensities of the emission luminescence peaks.

To further validate the specific effect and advantages of the mannan coating on UCNPs uptake, we conducted an inhibition assay to demonstrate MR-mediated internalization of C-M30 and S-M30 (Fig. 7A). For MR inhibition, mannan (1 or 10 mg mL^{-1}) was used, following established protocols.[54–56] A significant decrease in mean fluorescence intensity (MFI) was observed after 2 h, following a 30 min pre-treatment with either 1 mg mL^{-1} mannan for both C-M30 ($p < 0.01$) and S-M30 ($p < 0.0001$), or with 10 mg mL^{-1} mannan for C-M30 and S-M30 (both $p < 0.0001$) (Fig. 7B).

As an additional confirmation of the specific uptake of mannan-coated UCNPs by phagocytic cells expressing the MR, we tested the uptake of S-M30 in four non-phagocytic cell lines without MR expression and compared it with internalization in J774A.1 cells. Minimal internalization was observed in all MR-negative cell lines compared to J774A.1 cells (Fig. 8).

Experimental

Materials and methods

Chemicals. The rare earth oxides Y_2O_3, Yb_2O_3, and Er_2O_3, sodium trifluoroacetate ($NaCF_3COO$), trifluoroacetic acid (TFA, 99%), oleic acid (OA, 65.0–88.0%), 1-octadecene (ODE, 90%), and cyclohexane (99%) were purchased from Sigma-Aldrich (Warsaw, Poland). Inulin from chicory, mannan from *Saccharomyces cerevisiae*, sodium cyanoborohydride (95%), and sodium azide (99.5%) were purchased from Merck (Prague, Czech Republic); sodium periodate (99.0%) was purchased from HiChem (Prague, Czech Republic); hydrogen peroxide (30% not stabilized) was obtained from Lach-Ner (Neratovice, Czech Republic); AF 488 amine was purchased from Lumiprobe (Hanover, Germany). Sodium neridronate (Ner) was synthesized as described elsewhere.[4]

Synthesis of lanthanide trifluoroacetate ($Ln(TFA)_3$) precursors. $Ln(TFA)_3$ (Ln = Y, Yb, or Er) precursors were synthesized by dissolving 4 mmol of Y_2O_3, Yb_2O_3, or Er_2O_3 in a solution of 20 mL water and 20 mL trifluoroacetic acid. The mixture was

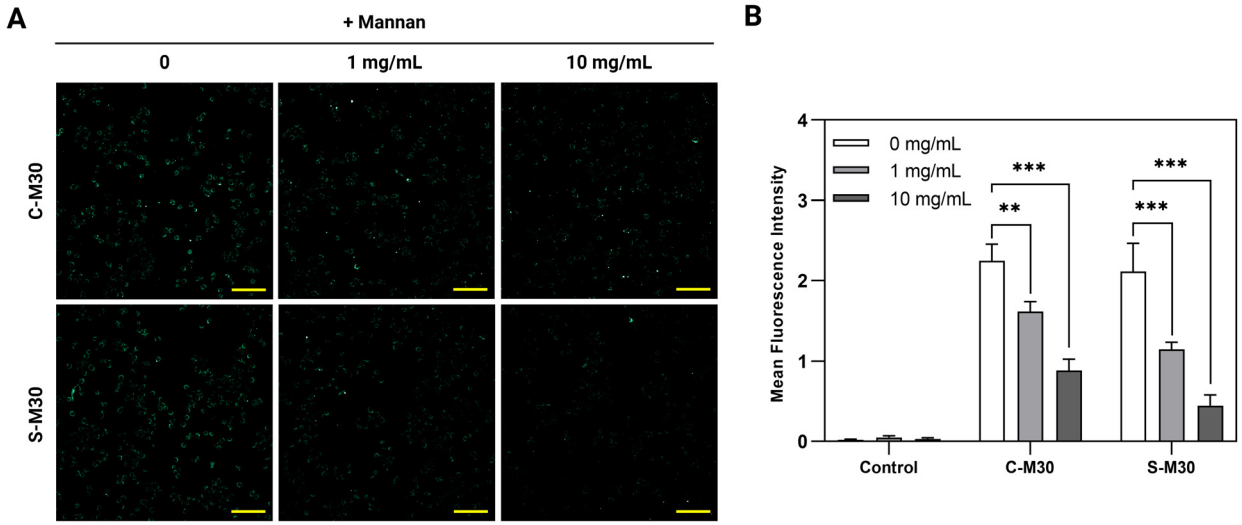

Fig. 7 Inhibition of MR-mediated uptake of UCNPs. (A) Confocal microscopy images of MR inhibition by mannan (1 or 10 mg mL^{-1}) after 2 h of treatment with C-M30 and S-M30 (green channel represents AF 488 signal). (B) Statistical analyses of UCNPs uptake inhibition (mean ± SD). *P*-Values were calculated using two-way ANOVA—Tukey's test, ** $p < 0.01$; **** $p < 0.0001$; $n = 3$. Scale bar: 100 μm.

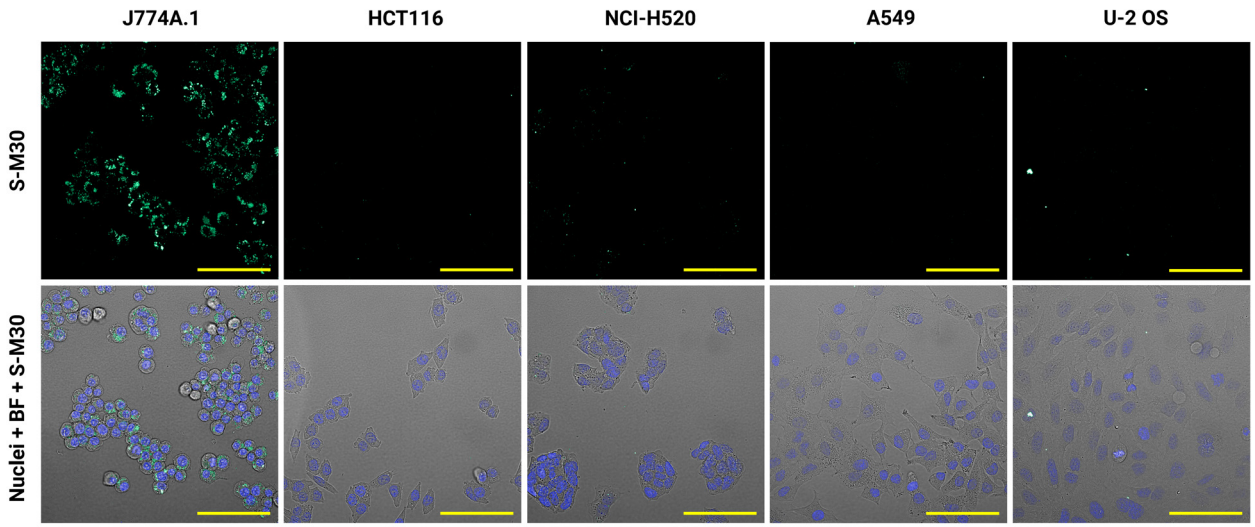

Fig. 8 UCNPs internalization in MR-negative non-phagocytic cell lines. Confocal microscopy images of J774A.1 cells and various non-phagocytic cell lines (HCT116, H520, A549, and U2OS) lacking MR expression, following 24 h incubation with S-M30 (5 μg mL^{-1}). Green channel: AF 488 signal of S-M30; blue channel: nuclei (Hoechst 33342). BF = Bright Field; $n = 3$. Scale bar: 100 μm.

stirred at boiling temperature until a transparent solution formed, then filtered to remove unreacted oxides. The filtrate was heated to evaporate water, and the resulting precipitate was dried at 120 °C in air for 12 h to obtain solid $Ln(TFA)_3$ powder.

Synthesis of Core β-$NaYF_4$:20%Yb^{3+},2%Er^{3+} and Core–Shell $NaYF_4$:20%Yb^{3+},2%Er^{3+}@$NaYF_4$ UCNPs. β-$NaYF_4$:20%Yb^{3+},2%Er^{3+} UCNPs were synthesized using a modified thermal decomposition method under strictly anhydrous and anaerobic conditions. In a 50 mL three-necked flask, the following precursors were mixed: $Y(CF_3COO)_3$ (0.78 mmol), $Yb(CF_3COO)_3$ (0.20 mmol), $Er(CF_3COO)_3$ (0.02 mmol), and $NaCF_3COO$ (2.5 mmol). Oleic acid (20 mmol) and 1-octadecene (20 mmol) were added to the mixture. The reaction mixture was degassed with argon for 30 min, then heated to 120 °C for 60 min to remove water. The reaction mixture was then heated to 330 °C for 30 min to synthesize the nanocrystals. After cooling, the nanocrystals were precipitated by adding ethanol and centrifuged at 6000 rpm for 10 min. The precipitate was dissolved in cyclohexane by sonication, then reprecipitated with excess ethanol, and this process was repeated 3–5 times. The final UCNPs were centrifuged, suspended in 5 mL of cyclohexane, and stored at room temperature. To obtain homogeneous and hexagonal core–shell nanoparticles, the same procedure was repeated without doping ions to form the shell.

Removal of oleic acid (OA). OA-coated core and OA-coated core–shell UCNPs were precipitated from 0.5 mL of cyclohexane with 1 mL of ethanol and centrifuged at 6000 rpm at 15 °C for 10 min. The UCNPs were then suspended in 0.1 M hydrochloric acid and sonicated for 180 min, then centrifuged at 16 500 rpm at 15 °C for 20 min and redispersed in ethanol–hydrochloric acid solution (pH 4) with sonication for an additional 180 min. This procedure was repeated five times using 99.8% ethanol, followed by five repetitions with sterile distilled water. Finally, the OA-free UCNPs were suspended in 1 mL of sterile distilled water.

Reductive amination for grafting of sodium neridronate (Ner) onto polysaccharides. To 250 mg of inulin or mannan (1.54 mmol of SMUs), dissolved in 20 mL of deionized water, solid sodium periodate (33 mg, 0.154 mmol or 99 mg, 0.462 mmol) was added to achieve oxidation of 10% or 30% of the SMUs, respectively. The solution was stirred in darkness at ambient temperature for 12 h. Subsequently, sodium neridronate (46 mg, 0.154 mmol or 138 mg, 0.462 mmol, respectively) and sodium borohydride (9 mg, 0.154 mmol or 27 mg, 0.462 mmol, respectively) were added as solids. The pH of the solution was adjusted to 6 using potassium hydroxide, and the mixture was stirred for another 12 h. The entire reaction mixture was freeze-dried, then dissolved in 3 mL of deionized water, purified by SEC on a Sephadex G25 column, and freeze-dried again. ^{1}H NMR (400 MHz, D_2O, δ), inulin: 4.22 (t, 1H); 4.08 (t, 1H); 3.84–3.70 (m, 5H); 3.03 (t, 2H); 1.87–1.67 (m, 2H), 1.61–1.37 (m, 4H); 1.32–1.17 (m, 2H); mannan: 5.26 and 5.06 (s and m, respectively, 1H); 4.23 (s, 1H); 4.05–3.76 (m, 5H); 3.03 (t, 2H); 1.87–1.67 (m, 2H), 1.61–1.37 (m, 4H); 1.32–1.17 (m, 2H).

Labelling of mannan and inulin with AF 488 amine by reductive amination. To a solution of inulin or mannan (20 mg, 0.12 mmol of SMUs) in 0.5 mL of deionized water, solid sodium periodate (2 mg, 9 μmol) was added to oxidize 8% of the saccharide monomer units. The reaction mixture was stirred overnight in the dark. Subsequently, AF 488 amine (0.2 mg, 0.3 μmol) and sodium cyanoborohydride (0.6 mg, 9 μmol), each dissolved in 40 μL of deionized water, were added. After overnight stirring, the AF 488 dye bleached in the presence of the reducing agent. To partially recover the fluorescence, 10 μL of 30% hydrogen peroxide was added. The polysaccharide was then purified by size-exclusion chromatography (SEC) on a Sephadex G-25 column and freeze-dried. The AF 488 content was determined colorimetrically in a 0.5 mg mL^{-1} solution of the polysaccharide in deionized water (ε_{495} = 71 800 L mol^{-1} cm^{-1}).

Adsorption of inulin and mannan on UCNP-C and UCNP-S. The aliquots from the dispersions of pristine nanoparticles in deionized water were mixed with pure water to achieve a final concentration of 1 mg mL^{-1}. To 200 μL of the diluted nanoparticle dispersion, 1 mg of polysaccharide grafted with Ner, or grafted with both Ner and AF 488, was added. The mixture was stirred overnight and purified from non-adsorbed polysaccharides using a centrifugal concentrator (MWCO 300 000, Vivaspin 500, Sartorius) at 268*g* for 20 min. The initial volume was concentrated to 20 μL, after which 180 μL of a 0.02% (w/v) aqueous solution of sodium azide was added. The nanoparticles were redispersed by repeated shaking. The centrifugation process was repeated three times, and the samples were stored as a dispersion in a 0.02% (w/v) sodium azide solution. The concentration of nanoparticles after purification was determined from the yttrium content in a weighed aliquot of 10 μL.

Characterization analyses

Scanning electron microscopy, transmission electron microscopy, energy dispersive X-ray spectroscopy, and electron diffraction. Scanning electron microscopy (SEM) studies were conducted using a ThermoFisher Scientific Helios 5 UX dual-beam scanning electron microscope. Transmission electron microscopy (TEM) studies were performed using a JEOL JEM-F200 microscope operated at 200 kV and equipped with a dual SDD energy-dispersive X-ray spectroscopy (EDS) system. Samples for TEM observations were prepared *via* drop-casting a nanoparticle suspension onto Lacey carbon TEM grids.

Nuclear magnetic resonance spectroscopy (^{1}H NMR). ^{1}H NMR spectra were acquired using a Bruker Avance NEO 400 spectrometer operating at 400.1 MHz. The width of the ^{1}H NMR 90° pulse was 16.5 μs, with a relaxation delay of 10 s, an acquisition time of 3.28 s, and 64 scans. All samples were dissolved in deuterated water and recorded at 323 K, following a 15 min stabilization period after the temperature was reached. The chemical shift was calibrated on the HDO signal according to[57] at 4.5 ppm.

Size exclusion chromatography (SEC) analysis. The SEC analyses were performed using a Deltachrom SDS 030 pump (Watrex Ltd, Prague, Czech Republic) with a 0.5 mL min^{-1} flow rate and a PL aquagel column, 8 μm, OH-MIXED-H (Polymer Laboratories, Shropshire, UK). A DAWN HELEOS II MALS detector (Wyatt Technology Corp.) with the laser operating at a wavelength λ = 658 nm, and an Optilab T-rEX differential refractometer (Wyatt Technology Corp.) were used in a series, respectively. Water (prepared with the laboratory water purification system Milli-Q® IQ 7000, Merck KGaA, Darmstadt, Germany) with the addition of 0.1 M LiCl (95%, Lachema, Czech Republic) was used as the mobile phase at ambient temperature. Manual injection was used and data were collected into Astra software (Wyatt Technology Corp.). $Đ$, M_w, and M_n were determined. The values of dn/dc used were set according to the literature 0.14 for inulin[58] and 0.145 for mannan.[59]

UV-Vis spectroscopy. UV-Vis spectra of polysaccharides with grafted AF 488 were recorded in 0.5 mg mL^{-1} solutions in deionized water using an Evolution 220 UV-Visible Spectrophotometer (Thermo Scientific, USA) in a glass cuvette.

Spectroscopic characterization of AF 488 and UCNPs. The emission spectra of AF 488 label and UCNPs were recorded using a FluoTime 300 fluorescence steady-state and lifetime spectrofluorometer equipped with a PDL 820 computer-controlled driver (PicoQuant GmbH, Berlin, Germany). The AF 488 label was excited with a SOLEA supercontinuum tunable laser

at 488 nm, while the UCNPs were excited with a LDH-D-C-980 diode laser head at 980 nm. Emission spectra were acquired using a PMA hybrid photon detector and high-resolution excitation and emission double monochromators. The measurement setup was automatically optimized and maintained across all series. Data were analysed with EasyTau software (version 2.2.3293, PicoQuant GmbH, Berlin, Germany). All measurements were performed at ambient temperature. Photoluminescence measurements of bare core–shell UCNPs (without mannan or inulin coating) dispersed in cyclohexane were performed using a spectral system with a continuous-wave (CW) 980 nm laser (Lumics LU0980D300-DNA014) as the excitation source and a spectrophotometer (Horiba Jobin Yvon Fluorolog3) as the detector.

X-ray photoelectron spectroscopy (XPS). XPS measurements were carried out with a K-Alpha$^+$ spectrometer (ThermoFisher Scientific, East Grinstead, UK). Neat UNCPs and their modified counterparts bearing inulin and mannan with grafted Ner have been spread on silicon wafers. The resulting films were analysed using a micro-focused (spot radius of 400 μm), monochromated Al Kα X-ray source at an angle of incidence of 30° (measured from the surface) and an emission angle normal to the surface. The kinetic energy of the electrons was measured using a 180° hemispherical energy analyser operated in the constant analyser energy mode (CAE) at 200 eV and 50 eV pass energy for the survey and high-resolution spectra respectively. Survey and high-resolution spectra were measured. The high-resolution spectra were measured in the region of 180–120 eV (covering the Y 3d, Si 2s and P 2p regions), C 1s, N 1s, O 1s, F 1s and Na 1s and survey spectra were measured. Spectral resolutions of 0.1 and 1.0 eV were used for the high-resolution and survey spectra, respectively. All reported XPS spectra are averages of the 10 individual measurements referenced to the C 1s peak of hydrocarbons at 285.0 eV. Data acquisition and processing were performed using Thermo Advantage software. The XPS spectra were fitted with Voigt profiles obtained by convolving Lorentzian and Gaussian functions. The analyser transmission function, Scofield sensitivity factors, and effective attenuation lengths (EALs) for photoelectrons were applied for quantification. EALs were calculated using the standard TPP-2M formalism. The BE scale was controlled by the well-known position of the photoelectron C–C and C–H, C–O and C(=O)–O C 1s peaks of polyethylene terephthalate and Cu 2p, Ag 3d, and Au 4f peaks of metallic Cu, Ag and Au, respectively. The BE uncertainty of the reported measurements and analysis is in the range of ±0.1 eV. The quantitative analysis and reported values are averages of 5 measurements on independently prepared samples.

Fluorescence correlation spectroscopy (FCS) analysis. Measurements of UCNP-C and UCNP-S, coated with I-10, M-10, and M-30, and carrying the AF 488 label, were performed using an Olympus IX83 confocal laser scanning microscope controlled by FluoView 1200 software (Olympus Corporation, Japan). This system was extended with a FLIM/FCS upgrade kit, operated using SymphoTime64 software (PicoQuant GmbH, Germany). The labelled UCNPs were excited by an LDH-D-C-485 laser diode emitting 488 nm light, driven by a PDL 828 Sepia II driver in picosecond pulsed mode at a 40 MHz repetition rate (both devices PicoQuant GmbH) through the 488 nm dichroic mirror built into the IX83 scan head. An Olympus UPlanSApo water immersion objective (60×, 1.2 NA) delivered the excitation light into a diffraction-limited spot and collected the emitted fluorescence. The laser intensity was maintained at approximately 2 μW average power at the objective entrance pupil to avoid photobleaching and/or saturation. The collected fluorescence passed through a Semrock 520 nm BrightLine emission filter and was detected by a hybrid photomultiplier (PMA Hybride-40 from PicoQuant GmbH) operated in photon counting mode. Photon counts were recorded using a PicoHarp300 TCSPC module in a T3 time tagging mode. The SymPhoTime64, ver. 2.1 software from PicoQuant was used for data acquisition and FCS data analysis. Each acquisition took 1–2 min in average, and the measurements were performed at 23 ± 1 °C. From the collected data, the number-weighted diffusion coefficient of AF 488 was calculated and then converted into the apparent hydrodynamic radius using the Einstein–Stokes equation.

Elemental analysis. Quantitative determination of yttrium (Y) in the samples was performed using an ICP-MS instrument (NexION 2000 B, PerkinElmer, USA). A standard solution of Y (c = 100 mg L^{-1}, 5% HNO_3; ANALYTIKA® spol. s r.o., Czech Republic) was used for calibration. Samples and standards were diluted to appropriate concentrations for ICP-MS analysis using Milli-Q grade water containing 2.5% nitric acid (65–69%, Analpure Ultra; ANALYTIKA® spol. s r.o.). The calibration curve for Y was established in standard mode over a concentration range of 0.04–0.97 μg L^{-1}. The phosphorus content was measured colorimetrically at 690 nm by molybdenum blue method on Biochrom Libra S22 UV-VIS spectrometer (Biochrom Ltd UK). The sample was dissolved in 1 mL $HClO_4$ and 0.3 mL HNO_3 in Biotage Initiator microwave reactor (Biotage AB, Sweden), then the aliquot of the solution was diluted with Milli-Q water. A reagent mixture containing H_2SO_4, ammonium molybdate, ascorbic acid, and antimony potassium tartrate was added, and absorbance was measured at 690 nm. Calibration was carried out using a certified phosphorus reference material (Astasol).

Dynamic light scattering (DLS). The hydrodynamic diameters of UCNP-C and UCNP-S, dispersed in DMEM cell culture medium (Carpicorn Scientific, Germany) at a concentration of 50 μg mL^{-1}, were measured at 37 °C using the Nano-ZS Zetasizer ZEN3600 Model (Malvern Instruments, UK).

In vitro experiments

Cell culture. J774A.1 cells (TIB-67™), U-2 OS (HTB-96™), HCT116 (CCL-247™), H520 (HTB-182™) and A549 (CCL-185™) were purchased from the American Type Culture Collection (ATCC). Cells were cultured in the appropriate ATCC-recommended medium supplemented with 10% foetal bovine serum (FBS) and 100 U mL^{-1} penicillin–streptomycin (Gibco™), and maintained at 37 °C in a humidified atmosphere containing 5% CO_2.

Cell viability assay. To evaluate cytotoxicity of the tested UCNPs a CellTiter 96 AQueous One Solution Cell Proliferation Assay (Promega G3580) was performed according to the manufacturer's protocol. The J774A.1 cells were seeded in clear 96-well plates (TPP) at 1×10^4 cells per well and incubated 24 h at 37 °C, 5% CO_2. Four different concentrations of UCNPs were tested: 0.5; 1; 5 and 10 μg mL^{-1}. All treatments were carried out in biological triplicate, each comprised of a technical triplicate. Cell viability was assessed 24 and 48 h post-treatment. Untreated cells were utilized as negative control (NC), while the positive controls were represented by cells treated with 10 μM Actinomycin D and 10 μM Mitomycin C. The absorbance from the corresponding cell-free conditions was used as background. The relative cell viability (%) was calculated using the formula: $[(ABS_{sample} - ABS_{background})/(ABS_{NC} - ABS_{background})] \times 100\%$.

Oxidative stress. To assess UCNP-induced oxidative stress in J774A.1 cells, two luminescence-based assays—ROS-Glo™ H_2O_2 Assay (Promega, G8820) and GSH-Glo™ Glutathione Assay (Promega, V6911) were performed according to the manufacturer's protocol. J774A.1 cells were seeded in white opaque 384-well plates (Revvity) at a density of 2.5×10^3 cells per well and incubated for 24 h at 37 °C with 5% CO_2.

The tested concentrations of UCNPs and the number of biological and technical replicates were identical to those described in the "*Cell viability assay*" section. Cellular levels of ROS and GSH were quantified 24 h post-treatment. For positive controls *i.e.*, increased H_2O_2 levels and decreased levels of GSH, cells were treated with 6.25, 12.5, or 25 μM menadione 6 h prior to the ROS-Glo™ H_2O_2 Assay and GSH-Glo™ Glutathione Assay readouts. Untreated cells were used as the negative control (NC). Luminescence from corresponding cell-free conditions was used as the background. Fold changes in H_2O_2 and GSH levels were calculated using the formula: $(LUM_{sample} - LUM_{background})/(LUM_{NC} - LUM_{background})$.

Imaging of UCNPs internalization. For live-cell imaging of UCNPs internalization, 1×10^4 J774A.1 cells per well were seeded in a PhenoPlate-96 (Revvity) and cultured for 24 h at 37 °C under 5% CO_2. The medium was completely replaced with fresh medium with or without UCNPs (1, 5, or 10 μg mL^{-1}) before confocal microscopy imaging. Live-cell imaging was performed using a Cell Voyager CV8000 high-throughput cellular imaging and discovery system (Yokogawa) at 37 °C in 5% CO_2 for 24 h. Time-lapse live imaging of UCNPs internalization was performed by acquiring images every 2 h. Bright-field and Alexa Fluor 488 (green channel: ex 488 nm; em 525/50 nm) images were acquired using a 20× or 40× water immersion objective. After live-cell imaging, cells were washed three times with ice-cold PBS followed by 15 min fixation with 4% paraformaldehyde at room temperature. Subsequently, one wash with PBS was performed. Finally, Hoechst 33342 in PBS (10 μM) was added for 15 min to the cells prior to imaging. Images of cells, following washing and fixation to remove non-internalized UCNPs, were acquired using a Cell Voyager CV8000 high-throughput cellular imaging and discovery system (Yokogawa) in the same setup as mentioned above with an additional channel added for Hoechst 33342 (ex 405 nm; em 445/45 nm). Image quantification for UCNPs internalization in live/fixed cells was calculated as the mean gray value per field (3 representative images) in the green channel. All images were post-processed and analysed using Signals Image Artist software (v1.3, Revvity) or ImageJ. Maximum intensity 3D projections of *z*-stack images are presented.

Optical and immunocytochemical analysis using confocal microscopy. Cells were seeded onto chamber slides (Thermo Scientific) at 4×10^4 cells per well and incubated for 24 h at 37 °C in a humidified atmosphere with 5% CO_2. The medium was then completely replaced with fresh medium containing UCNP-C-M30 or UCNP-S-M30 (5 μg mL^{-1}), or without nanoparticles (control).

After 4 h of incubation, cells were washed three times with PBS and fixed for 15 min at room temperature using 4% paraformaldehyde. Permeabilization was carried out with 0.25% Triton X-100 in PBS for 15 min, followed by a single PBS wash. Cells were then blocked for 90 min with 1% BSA in PBS, which was also used for dilution of both primary and secondary antibodies. After blocking, primary anti-human Rab7 monoclonal antibody D95F2 (1 : 200, Cell Signaling) was added, and cells were incubated overnight at 4 °C.

The following day, all wells were washed three times with PBS and incubated with goat anti-rabbit IgG (H + L) Cross-Adsorbed Secondary Antibody, Alexa Fluor 647 (1 : 1000, Invitrogen) for 60 min at room temperature, followed by three additional washes. Finally, Hoechst 33342 in PBS (10 μM) was added for 15 min to stain the nuclei.

The intracellular presence, subcellular colocalization, and luminescence properties of UCNPs were assessed using an LSM 710 NLO microscope (Carl Zeiss), equipped with an infrared femtosecond laser (Chameleon, Coherent). UCNPs were excited with a femtosecond laser at a wavelength of 980 nm (red channel; em 500–700 nm), or with an argon laser at a wavelength of 488 nm for AF 488 signal (green channel; em 494–572 nm), Hoechst 33342 (cell nuclei) were excited with a femtosecond laser at a wavelength of 705 nm (blue channel; em 425–475 nm), and Rab7 (late endosomes) were excited with an argon laser at a wavelength of 633 nm (red channel; em 644–722 nm).

Inhibition of MR-mediated UCNPs internalization. To inhibit MR-mediated internalization of UCNPs, cells were pre-incubated with mannan (Sigma-Aldrich). Cells were seeded as described above in the section "*Imaging of UCNPs Internalization*". At 24 h post-seeding, the culture medium was replaced with fresh medium containing 1 mg mL^{-1} or 10 mg mL^{-1} of mannan, or without mannan (control), and incubated for 30 min. Subsequently, UCNP-C-M30 or UCNP-S-M30 (both at 5 μg mL^{-1}) in complete medium was added. Live-cell imaging was performed using a Cell Voyager CV8000 high-throughput cellular imaging and discovery system (Yokogawa) after 2 h of incubation at 37 °C in 5% CO_2. Bright-field and green channel images (ex 488 nm; em 525/50 nm) were captured by a 20× water immersion objective. The inhibition of UCNP internalization was quantified by measuring the mean

gray value per field in the green channel, using ImageJ software. All images were post-processed and analysed using Signals Image Artist software (version 1.3, Revvity) and ImageJ. Maximum 3D projections of *z*-stacks are presented.

UCNPs uptake in non-phagocytic cells lacking MR expression. Various cell lines, including J774A.1, U-2 OS, HCT116, H520, and A549, were seeded as described in the "*Imaging of UCNPs Internalization*" section. The culture medium was replaced with fresh medium, with or without UCNP-C-M30 or UCNP-S-M30 (5 μg mL^{-1}). After 24 h of incubation, the cells were washed three times with PBS and fixed for 15 min at room temperature using 4% paraformaldehyde. Following fixation, the cells were washed once with PBS. Hoechst 33342 (10 μM) in PBS was then added for 15 min to stain the nuclei before imaging. Images of fixed cells were acquired using a Cell Voyager CV8000 high-throughput cellular imaging and discovery system (Yokogawa) in the same setup as mentioned above.

Statistical analysis

In vitro imaging quantification data of UCNP internalization and inhibition calculations are presented as mean ± standard deviation ($n = 3$). Data acquired from maximum 3D projections of *z*-stacks are presented. All experiments were done in at least three biological replicates. The results were analysed using one-way ANOVA followed by Dunnett's *post hoc* test or two-way ANOVA followed by Tukey's *post hoc* test, using GraphPad Prism 8.0 software. For all analyses, a *p*-value ≤ 0.05 was considered statistically significant.

Conclusions

In this work, we developed colloidally stable and biologically functional UCNPs by coating them with hydroxybisphosphonate-modified polysaccharides—specifically, inulin and mannan. This surface engineering strategy provided both strong anchoring to the UCNPs and enhanced steric and electrostatic stabilization in biologically relevant media, effectively preventing aggregation and preserving upconversion luminescence.

Mannan-functionalized UCNPs showed significantly enhanced uptake in MR-expressing macrophage-like J774A.1 cells compared to inulin-coated analogues. Confocal microscopy, receptor inhibition assays, and Rab7 colocalisation studies confirmed that the uptake occurs *via* mannose receptor-mediated endocytosis and subsequent endo–lysosomal trafficking. Importantly, the particles retained their photophysical properties following surface modification, and cytotoxicity assays demonstrated good biocompatibility across a range of concentrations (with no significant cytotoxic effects observed in J774A.1 cells, even at higher concentrations 10 μg mL^{-1}).

These findings establish hydroxybisphosphonate-functionalized mannan as a promising coating for the targeted delivery of UCNPs to MR-expressing immune cells, such as macrophages. The combination of optical stability, minimal cytotoxicity, and receptor-specific cellular uptake supports their further development for *in vivo* biomedical imaging and targeted therapeutic applications.

Author contributions

Karolina Zajdel – funding acquisition, conceptualization, methodology, investigation (synthesis and preparation of UCNPs), visualization, formal analysis, project administration, writing – original draft, writing – review & editing; Volodymyr Lobaz – methodology, investigation (characterization: modification of polysaccharides, stabilization of UNCPs, DLS), formal analysis, data curation, writing – original draft, writing – review & editing; Martin Ondra – methodology, investigation (*in vitro* experiments: confocal microscopy, receptor blocking, immunocytochemistry), data curation, formal analysis, visualization, writing – original draft, writing – review & editing; Rafal Konefał – characterization (NMR measurement and interpretation), Oliver Moravec – investigation (characterization: PL and FCS), formal analysis; Ognen Pop-Georgievski – investigation (XPS), formal analysis; Jiří Pánek – investigation (characterization: PL and FCS), formal analysis; Damian Kalita – investigation (TEM, SEM, EDS, Electron Diffraction), formal analysis; Bożena Sikora-Dobrowolska – investigation (confocal analysis), formal analysis; Lukáš Lenart – data curation, investigation (*in vitro* experiments: cell viability and oxidative stress), writing – review & editing; Marián Hajdúch – funding acquisition, writing – review & editing, conceptualization, supervision; Martin Hrubý – funding acquisition, conceptualization, writing – original draft, supervision; Marek Pruszyński – conceptualization, supervision, writing – review & editing.

Conflicts of interest

There are no conflicts to declare.

Data availability

The data supporting this article have been included as part of the supplementary information (SI). The Supplementary Information includes additional physicochemical characterizations such as EDS analysis, NMR spectra, photoluminescence spectra, and DLS measurements of the studied nanoparticles. It also presents results of their interactions with cells obtained by confocal microscopy, including uptake kinetics and *Z*-stack analysis. See DOI: https://doi.org/10.1039/d5nr01833a.

Acknowledgements

This research was funded in part by National Science Centre, Poland (Grant No. 2024/52/C/ST5/00208). This work was

carried out in part within the framework of the NOMATEN Centre of Excellence, supported from the European Union Horizon 2020 research and innovation program (Grant Agreement No. 857470) and from the Ministry of Science and Higher Education's initiative "Support for the Activities of Centers of Excellence Established in Poland under the Horizon 2020 Program" (Agreement No. MEiN/2023/DIR/3795). This study was supported by the Ministry of Education, Youth and Sports of the Czech Republic (grant LUAUS24272 and European Infrastructure for Translational Medicine—EATRIS-CZ, Project No. LM2023053) and the National Institute for Cancer Research —Program EXCELES, ID Project No. LX22NPO5102, funded by the European Union—Next Generation EU. Furthermore, this research project was also supported by the National Infrastructure for Biological and Medical Imaging (Czech-BioImaging) and by the Ministry of Health of the Czech Republic (grant AZV # NW24-03-00387). This work has been done in the NanoFun laboratories co-financed by the European Regional Development Fund with the Innovation Economy Operational Program no. POIG.02.02.00-00025/09/. Graphical abstract, Fig. 4–8, and Fig. S7 were created in BioRender. Ondra, M. (2025). Graphical abstract, https://BioRender.com/9r7k3s5; Fig. 4, https://BioRender.com/u9zb1mk; Fig. 5, https://BioRender.com/flz4gk7; Fig. 6, https://BioRender.com/ev74zu8; Fig. 7, https://BioRender.com/adnv2h6; Fig. 8, https://BioRender.com/j5zjowl; Fig. S7, https://BioRender.com/9hj0o4z.

References

1 M.-X. Zhao and E.-Z. Zeng, *Nanoscale Res. Lett.*, 2015, **10**, 171.
2 J. B. Oehler, W. Rajapaksha and H. Albrecht, *J. Pers. Med.*, 2024, **14**, 723.
3 J. Yoon, X. T. Le, J. Kim, H. Lee, N. T. Nguyen, W. T. Lee, E. S. Lee, K. T. Oh, H.-G. Choi and Y. S. Youn, *J. Controlled Release*, 2023, **360**, 482–495.
4 U. Kostiv, V. Lobaz, J. Kučka, P. Švec, O. Sedláček, M. Hrubý, O. Janoušková, P. Francová, V. Kolářová, L. Šefc and D. Horák, *Nanoscale*, 2017, **9**, 16680–16688.
5 C. Xu, S. K. Law and A. W. N. Leung, *Pharmaceuticals*, 2024, **17**, 663.
6 R. S. Ajee, P. S. Roy, S. Dey and S. Sundaresan, *J. Nanopart. Res.*, 2024, **26**, 50.
7 S. Liu, Z. An and B. Zhou, *Chem. Eng. J.*, 2023, **452**, 139649.
8 K. Du, J. Feng, X. Gao and H. Zhang, *Light: Sci. Appl.*, 2022, **11**, 222.
9 R. Rafique, S. K. Kailasa and T. J. Park, *TrAC, Trends Anal. Chem.*, 2019, **120**, 115646.
10 J. Kim, S. Lee, Y. Jeong, K. Kim, K. Nam, H. Jin, Y. Choi, H. Kim, H. Ryu, K. H. Kim, J. Kim, J. Park, J. Joo and J. Park, *Adv. Mater.*, 2025, **37**, 2502739.
11 N. Akhtar, P.-W. Wu, C. L. Chen, W.-Y. Chang, R.-S. Liu, C. T. Wu, A. Girigoswami and S. Chattopadhyay, *ACS Appl. Nano Mater.*, 2022, **5**, 7051–7062.
12 Y. Jiang, Y. Hong, Y.-Y. Liu, Y. Guan, J. Zhou, H. Wang and L. Sun, *J. Mater. Chem. C*, 2024, **12**, 11938–11947.
13 N. Akhtar, C. L. Chen and S. Chattopadhyay, *Biomater. Adv.*, 2022, **141**, 213117.
14 C. Liu, H. Shao, D. Li, X. Sui, N. Liu, S. U. Rahman, X. Li and P. R. Arany, *Photodiagn. Photodyn. Ther.*, 2021, **36**, 102485.
15 H. Oliveira, A. Bednarkiewicz, A. Falk, E. Fröhlich, D. Lisjak, A. Prina-Mello, S. Resch, C. Schimpel, I. V. Vrček, E. Wysokińska and H. H. Gorris, *Adv. Healthcare Mater.*, 2019, **8**, 1801233.
16 D. Lisjak, O. Plohl, J. Vidmar, B. Majaron and M. Ponikvar-Svet, *Langmuir*, 2016, **32**, 8222–8229.
17 M. I. Saleh, B. Rühle, S. Wang, J. Radnik, Y. You and U. Resch-Genger, *Sci. Rep.*, 2020, **10**, 19318.
18 J. Schubert and M. Chanana, *Curr. Med. Chem.*, 2018, **25**, 4553–4586.
19 D. Przybylska and T. Grzyb, *J. Alloys Compd.*, 2023, **933**, 167708.
20 Y. Xu, S. Ma, J. Zhao, H. Chen, X. Si, Z. Huang, Z. Yu, W. Song, Z. Tang and X. Chen, *Biomaterials*, 2022, **284**, 121489.
21 B. Rastegari, A. Ghamar Talepoor, S. Khosropanah and M. Doroudchi, *ACS Omega*, 2024, **9**, 658–674.
22 M. Rabyk, A. Galisova, M. Jiratova, V. Patsula, L. Srbova, L. Loukotova, J. Parnica, D. Jirak, P. Stepanek and M. Hruby, *J. Mater. Chem. B*, 2018, **6**, 2584–2596.
23 R. Swami, P. Popli, K. Sal, R. R. Challa, B. Vallamkonda, M. Garg and C. P. Dora, *Int. J. Biol. Macromol.*, 2025, **306**, 141740.
24 Y. Miyake, *Microbiol. Immunol.*, 2025, **69**(5), 257–269.
25 D. M. Balkin, G. J. Tranah, F. Wang, C. O'Donoghue, E. A. Morell, C. Porubsky, M. Nosrati, E. M. Vaquero, H. Kim, M. J. Carr, J. L. Montilla-Soler, M. C. Wu, D. M. Torre, M. Kashani-Sabet, J. S. Zager and S. P. Leong, *Cancer Control*, 2023, **30**, 10732748231153775.
26 V. Lobaz, M. Hladik, M. Steinhart, A. Paruzel, P. Černoch, J. Pánek, M. Vetrík, D. Jirák, M. Jirátová, O. Pop-Georgievski, M. Šlouf, S. Garcia-Argote, G. Pieters, E. Doris and M. Hrubý, *J. Colloid Interface Sci.*, 2018, **512**, 308–317.
27 W. Li, K. Dong, H. Wang, P. Zhang, Y. Sang, J. Ren and X. Qu, *Biomaterials*, 2019, **217**, 119310.
28 Y. Liu, T. Kobayashi, M. Iizuka, T. Tanaka, I. Sotokawa, A. Shimoyama, Y. Murayama, E. Otsuji, S. Ogura and H. Yuasa, *Bioorg. Med. Chem.*, 2013, **21**, 2832–2842.
29 K. Zajdel, D. Bartczak, M. Frontczak-Baniewicz, D. A. Ramsay, P. Kowalik, K. Sobczak, I. Kamińska, T. Wojciechowski, R. Minikayev, H. Goenaga-Infante and B. Sikora, *Nanomedicine*, 2023, **18**, 233–258.
30 K. Zajdel, J. Janowska, M. Frontczak-Baniewicz, J. Sypecka and B. Sikora, *Int. J. Mol. Sci.*, 2023, **24**, 1122.
31 H. Li, L. Xu and G. Chen, *Molecules*, 2017, **22**, 2113.
32 S. Najmr, T. Lu, A. W. Keller, M. Zhang, J. D. Lee, M. Makvandi, D. A. Pryma, C. R. Kagan and C. B. Murray, *Nano Futures*, 2018, **2**, 025002.

33 X. Liang, J. Fan, Y. Zhao and R. Jin, *J. Cluster Sci.*, 2021, **32**, 1683–1691.
34 J. Ren, Y. Ding, H. Zhu, Z. Li, R. Dai, H. Zhao, X. Hong and H. Zhang, *ACS Appl. Nano Mater.*, 2022, **5**, 559–568.
35 S. S. Panikar, G. Ramírez-García, A. A. Vallejo-Cardona, N. Banu, O. A. Patrón-Soberano, D. Cialla-May, T. A. Camacho-Villegas and E. De La Rosa, *Nanoscale*, 2019, **11**, 20598–20613.
36 S. Namagal, N. V. Jaya, M. Muralidharan and S. Sumithra, *J. Mater. Sci. Mater. Electron.*, 2020, **31**, 11398–11410.
37 A. Lakshmanan, R. A. Akasov, N. V. Sholina, P. A. Demina, A. N. Generalova, A. Gangadharan, D. K. Sardar, K. B. Lankamsetty, D. A. Khochenkov, E. V. Khaydukov, S. V. Gudkov, M. Jayaraman and S. Jayaraman, *Nanomaterials*, 2021, **11**, 2234.
38 X. Chen, Z. Yang, Q. Chen and Y. Zhang, *Front. Bioeng. Biotechnol.*, 2023, **11**, 1168086.
39 G. Liu, J. Wei, X. Li, M. Tian, Z. Wang, C. Shen, W. Sun, C. Li, X. Li, E. Lv, S. Tian, J. Wang, S. Xu and B. Zhao, *Adv. Sci.*, 2022, **9**, 2202505.
40 S. Plunkett, M. El Khatib, İ. Şencan, J. E. Porter, A. T. N. Kumar, J. E. Collins, S. Sakadžić and S. A. Vinogradov, *Nanoscale*, 2020, **12**, 2657–2672.
41 M. W. Pin, E. J. Park, S. Choi, Y. I. Kim, C. H. Jeon, T. H. Ha and Y. H. Kim, *Sci. Rep.*, 2018, **8**, 2199.
42 V. Lobaz, R. Konefał, J. Pánek, M. Vlk, J. Kozempel, M. Petřík, Z. Novy, S. Gurská, P. Znojek, P. Štěpánek and M. Hrubý, *Colloids Surf., B*, 2019, **179**, 143–152.
43 U. Kostiv, Z. Farka, M. J. Mickert, H. H. Gorris, N. Velychkivska, O. Pop-Georgievski, M. Pastucha, E. Odstrčilíková, P. Skládal and D. Horák, *Biomacromolecules*, 2020, **21**, 4502–4513.
44 M. L. Fiani, J. Beitz, D. Turvy, J. S. Blum and P. D. Stahl, *J. Leukocyte Biol.*, 1998, **64**, 85–91.
45 S. A. Linehan, L. Martínez-Pomares, P. D. Stahl and S. Gordon, *J. Exp. Med.*, 1999, **189**, 1961–1972.
46 G. Loor, J. Kondapalli, J. M. Schriewer, N. S. Chandel, T. L. Vanden Hoek and P. T. Schumacker, *Free Radicals Biol. Med.*, 2010, **49**, 1925–1936.
47 K. Malhotra, B. Kumar, P. A. E. Piunno and U. J. Krull, *ACS Appl. Mater. Interfaces*, 2024, **16**, 35985–36001.
48 C. Kembuan, H. Oliveira and C. Graf, *Beilstein J. Nanotechnol.*, 2021, **12**, 35–48.
49 H. Mirmajidi, H. Lee, N. Nipu, J. Thomas, Z. Gajdosechova, D. Kennedy, J. A. Mennigen and E. Hemmer, *J. Mater. Chem. B*, 2025, **13**, 160–176.
50 Y. Han, H. Li, Y. Wang, Y. Pan, L. Huang, F. Song and W. Huang, *Sci. Rep.*, 2017, **7**, 1320.
51 L. Labrador-Páez, U. Kostiv, Q. Liu, Y. Li, H. Ågren, J. Widengren and H. Liu, *J. Phys. Chem. Lett.*, 2022, **13**, 11208–11215.
52 M. Haase and H. Schäfer, *Angew. Chem., Int. Ed.*, 2011, **50**, 5808–5829.
53 F. T. Rabouw, P. T. Prins, P. Villanueva-Delgado, M. Castelijns, R. G. Geitenbeek and A. Meijerink, *ACS Nano*, 2018, **12**, 4812–4823.
54 K. Kvakova, M. Ondra, J. Schimer, M. Petrik, Z. Novy, H. Raabova, M. Hajduch and P. Cigler, *Adv. Funct. Mater.*, 2022, **32**, 2109960.
55 J. Lai, O. K. Bernhard, S. G. Turville, A. N. Harman, J. Wilkinson and A. L. Cunningham, *J. Biol. Chem.*, 2009, **284**, 11027–11038.
56 S. Sung, R. Nelson and S. Silverstein, *J. Cell Biol.*, 1983, **96**, 160–166.
57 H. E. Gottlieb, V. Kotlyar and A. Nudelman, *J. Org. Chem.*, 1997, **62**, 7512–7515.
58 G. Nikolic, M. Cakic and L. Ilic, *J. Serb. Chem. Soc.*, 2001, **66**, 397–401.
59 M. S. Graus, M. J. Wester, D. W. Lowman, D. L. Williams, M. D. Kruppa, C. M. Martinez, J. M. Young, H. C. Pappas, K. A. Lidke and A. K. Neumann, *Cell Rep.*, 2018, **24**, 2432–2442.